MOX-Report No. 39/2020

Extended Finite Element Method for Fluid-Structure Interaction in Wave Membrane Blood Pumps

Martinolli, M.; Biasetti, J.; Zonca, S.; Polverelli, L.; Vergara, C.

Extended Finite Element Method for Fluid-Structure Interaction in Wave Membrane Blood Pumps[*]

Marco Martinolli[1], Jacopo Biasetti[2], Stefano Zonca[1], Luc Polverelli[2], Christian Vergara[3]

June 7, 2020

1 MOX– Modellistica e Calcolo Scientifico
Dipartimento di Matematica
Politecnico di Milano
`<marco.martinolli,stefano.zonca>@polimi.it`

2 CorWave SA, Clichy, France
`<jbiasetti83@gmail.com,luc.polverelli@corwave.com>`

3 Laboratory of Biological Structure Mechanics (LaBS)
Dipartimento di Chimica, Materiali e Ingegneria Chimica
Politecnico di Milano
`christian.vergara@polimi.it`

Keywords: Fluid-Structure Interaction, Wave membrane blood pump, Extended Finite Element Method, Model validation

Abstract

Numerical simulations of cardiac blood pump systems are integral to the optimization of device design, hydraulic performance and hemocompatibility. In wave membrane blood pumps, blood propulsion arises from the wave propagation along an oscillating immersed membrane, which generates small pockets of fluid that are pushed towards the outlet against an adverse pressure gradient. We studied the Fluid-Structure Interaction between the oscillating membrane and the blood flow via three-dimensional simulations using the Extended Finite Element Method, an unfitted numerical technique that avoids remeshing by using a fluid fixed mesh. Our three-dimensional numerical simulations in a realistic pump geometry highlighted the role of the membrane deformation in promoting a blood flow towards the outlet despite of a resistive pressure gradient. We also simulated the pump system at different pressure conditions and we validated the numerical results against *in-vitro* experimental data.

1

1   Introduction

Heart failure is a global pandemic disease that affects more than 26 million people worldwide, a number which will continue to increase in the next decades [1, 2]. To address this challenge, there is an increasing interest in developing reliable *mechanical circulatory support* devices which take over, totally or partially, the pumping function of the failing heart. These devices can be employed as bridge to heart transplantation or as destination therapy, to permanently support heart function.

Ventricular Assist Devices (VADs) [3, 4], which are designed to support the heart's ventricle function, are becoming the standard of care for patients with end-stage heart failure. In comparison to other devices (such as *total artificial hearts* [5]), VADs have proved to be less invasive, featuring better performance in terms of hemocompatibility and risk of adverse events [4].

In *Left-Ventricular Assist Devices* (LVADs), blood pumps collect the blood from the left ventricular chamber and eject it into the ascending aorta via a flexible cannula. The standard blood pumps currently available for clinical use are rotary pumps, based on the rotation of an internal impeller that imparts kinetic energy to the blood. Rotary pumps are divided in axial [6, 7] and centrifugal flow pumps [8, 9, 10], depending on the direction of the imparted blood acceleration [3]. However, rotary pumps cause damage to blood elements producing hemolysis, thrombosis, and bleeding complications because of the elevated velocity gradients of their rotors [11, 12]. Furthermore, since these pumps are operated at a single pump speed, their clinical use results in a reduction of patient pulse pressure and, consequently, to possible complications related to continuous non-physiologic blood pumping, such as gastro-intestinal bleeding, aortic valve insufficiency or stroke [4]. Therefore, LVAD companies have developed pulsation algorithms for rotary pumps, with the aim of improving wash-out in the pumps and reducing thrombosis. However, the LVAD pulsation algorithms currently used clinically do not restore a physiologic pulse [13].

With the aim to overcome the drawbacks of rotary pumps, CorWave SA (Clichy, France) is developing a novel LVAD, referred to as *wave membrane blood pump* or *progressive wave blood pump*, which employs an innovative pumping technology based on the gentle propelling action of an elastic membrane on the blood. Compared with current rotary VADs, wave membrane blood pumps have two major advantages: i) the membrane generates smaller shear stresses and may provoke less trauma on the blood cells; ii) due to the low inertia of the membrane, the oscillation frequency can be rapidly changed to alter hydraulic performance in order to get physiologic pulsatile flow, potentially reducing the risks of complications like stroke, non-surgical bleeding and renal dysfunction. This novel fluid propulsion approach requires a deep insight into the fluid-structure dynamics arising within the pump.

Mathematical modeling and numerical simulations are valuable tools in the field of cardiovascular medicine, allowing to better understand the complex pro-

cesses involved in cardiovascular diseases and to support clinical decisions in treatments and surgical procedures [14, 15, 16, 17]. Particularly, in the case of biomedical devices, computational simulations are widely used to investigate and optimize performance under different clinical conditions. Among others, we mention the following fields of application: the optimization of coronary arterial bypass grafts to reduce critical factors, like flow vorticity and wall shear stress rate [18, 19]; the study of blood dynamics in *transcatheter aortic valve*, a biological prosthesis that replaces the native aortic valve in patients with high-risk valve diseases [20, 21, 22, 23]; the performance of *drug-eluting stents*, which prevent restenosis by local releasing of a specific drug [24, 25, 26, 27]; the study of optimal anastomotic angle in arteriovenous fistula for hemodialysis [28, 29].

In the case of VADs, Computational Fluid Dynamics (CFD) has proven to be a powerful tool to improve the pump performance and efficiency, while reducing blood trauma. Indeed, starting in the 1990s with the first numerical studies carried out in simplified pump models [30, 31], *in silico* simulations emerged to be more time- and cost-effective than *in vitro* or *in vivo* testings, overcoming limitations in prototype fabrication and experimental setup [12]. In the last decades, there have been plenty of numerical studies concerning the design and performance of rotary blood pumps. Among these, we mention, for instance: parametric studies of geometric features in centrifugal [32, 33] and axial pumps [34], to analyze the effects on hydraulic efficiency and stagnation time; CFD-based optimization of the pump design to avoid retrograde leakage flow [35, 36]; computational study of the effect of the impeller position in a magnetically levitated blood pump [37]. Other works focused on the optimal implantation of the device [38, 39, 40, 41] or on the hemocompatibility requirements of VADs, trying to understand and prevent the mechanisms that favor hemolysis [42, 43, 44], thrombogenicity [45, 46, 47], and gastrointestinal bleeding [48].

Regarding progressive wave blood pumps, to our knowledge the only reference is the work from Perschall et al. [49], who performed a Fluid-Structure Interaction (FSI) study, providing a validation of their results against experimental data. The authors also proposed a new tubular configuration of the pump. FSI numerical experiments have been carried out by considering a 2D axi-symmetric approximation of the discoidal geometry. The fluid-structure dynamics are described through the coupling of incompressible Navier-Stokes (NS) equations, written in the Arbitrary Lagrangian-Eulerian (ALE) formulation, with linear elastodynamic equations. Moreover, a Design Of Experiment (DOE) method is applied to build a virtual prototype of the tubular design by the accurate tuning of geometric parameters, like membrane diameter, membrane thickness or pump walls angle.

The objective of this paper is to provide a significant step forward with respect to [49], by means of numerical investigation of the pump functioning in a three-dimensional pump domain for different key functional parameters. To this aim, we need to identify a numerical strategy that is able to accurately describe the behaviour of a thin wave membrane immersed in the blood flow,

which undergoes large displacements. Numerical methods for this FSI problems are divided in two main classes: fitted and unfitted mesh methods. In the former group, the fluid and the solid meshes are conforming. ALE technique [50, 51] and Space-Time Finite Elements [52, 53] belong to this family of methods. However, in case of large structural deformations, as it happens in wave membrane blood pumps, such methods may fail due to excessive distortion of the fluid mesh, requiring frequent remeshing procedures. On the contrary, unfitted methods are specifically designed to avoid remeshing issues by using a fixed background mesh for the fluid and an overlapping solid mesh which is free to move on the foreground, leading to split fluid mesh elements. The most important unfitted techniques are: Immersed Boundary (IB) [54, 55, 56], Fictitious Domain (FD) [57, 58, 59], Extended Finite Element Method (XFEM) [60, 61, 62], and polygonal Discontinuous Galerkin (PolyDG) method [63]. In the framework of XFEM, the degrees of freedom (d.o.f.) of the split elements are doubled so that the solution can be integrated independently in the two sub-regions, thus permitting an internal discontinuity [64]. Compared to the other unfitted methods, XFEM is more capable of capturing the fluid-structure interface without loss of accuracy in the coupling dynamics, but it is more complex to implement due to the intersection between the unfitted meshes. XFEM has already proven to be an effective, robust and versatile numerical strategy to solve FSI problems of thin immersed membranes, both in 2D [65, 66] and in 3D [67, 68]. For these reasons, in this work we adopted an XFEM-based strategy to handle the FSI problem arising in our progressive wave blood pump.

The structure of this paper is the following: in Section 2, we describe the working mechanisms of the wave membrane blood pump under study; in Section 3, we introduce the mathematical formulation of the FSI model together with its numerical discretization; in Section 4, we present the results of the numerical simulations for different pressure conditions and we validate the model against experimental data from real pump performance curves; in Section 5, we finally draw the main conclusions of the current study and we depict the possible future developments of the work.

2 Pump functioning principle

In case of heart failure, the cardiac function is compromised and only a reduced volume of oxygenated blood is ejected into circulation, leading to poor oxygenation of the tissues. Therefore, blood pumps are implanted at the apex of the failing heart to collect part of the blood from the left ventricle in the pump chamber and mechanically pump it into the distal aorta via a flexible outlet cannula (Figure 1, left). In particular, progressive wave pumps differ from standard blood ones for utilizing an innovative pumping mechanism based on the mutual interaction between an elastic undulating membrane and the blood flow, with

4

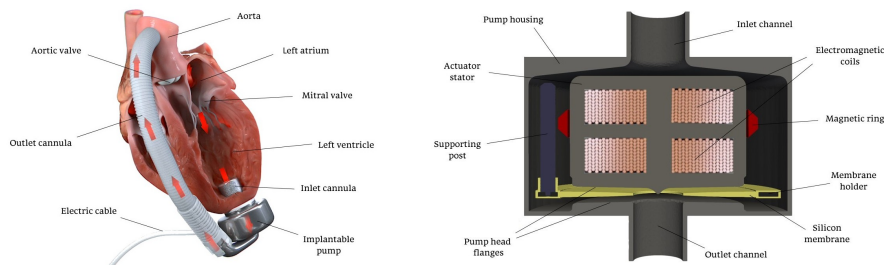the potential to produce physiologic flow rates with minimum blood trauma.

Figure 1: Left: Blood path through the left heart with an implanted LVAD. The oxygenated blood coming from the left atrium is collected into the implantable pump apparatus placed at the left ventricle apex, and then ejected into the proximal aorta via an outlet cannula. Right: Cross sectional view of the main components of the implantable wave membrane pump, including inlet and outlet channel, the central actuator (stator, electromagnetic coils and magnet ring), the membrane assembly (silicon membrane and membrane holder), and one (of the three) supporting posts.

The main components of the membrane wave pump are shown in the right panel of Figure 1 and correspond to the inlet and the outlet cannula, the actuator assembly and the membrane assembly. The inlet and the outlet channels are located at the opposite ends of the pump cylindrical body. The actuator assembly is composed of a stationary part, consisting of the central stator and the electromagnetic coils, and a mobile part, the *magnet ring*, that is suspended concentrically around the stator. The membrane assembly consists of the silicon membrane and the membrane holder. The silicon membrane is a discoidal polymer elastic body that is displaced concentrically to the pump axis, in the pump head region, i.e. a narrow space proximal to the outlet channel delimited by rigid walls of the pump housing, called *pump head flanges*. Both the gap between these flanges and the membrane thickness gradually decrease going towards the inner circular opening. The membrane holder is a rigid titanium ring that is enclosed in the most external part of the membrane disc and that is connected to the magnet ring by means of three supporting posts placed equidistantly over the actuator circumference.

The action of the blood pump is driven by the electromagnetic actuator which triggers the undulating motion of the flexible silicon membrane. An alternating current is applied to the coils to generate a magnetic field that guides the periodic displacement of the magnet ring and, consequently, of the membrane holder. Notice that the motion of the magnet ring is axially constrained because of the presence of suspension rings which do not permit radial displacements. In this way, the actuator exerts a periodic excitation force that is substantially normal to the membrane disc, inducing a wavelike displacement which propagates in the membrane medium from the membrane holder towards the center in di-
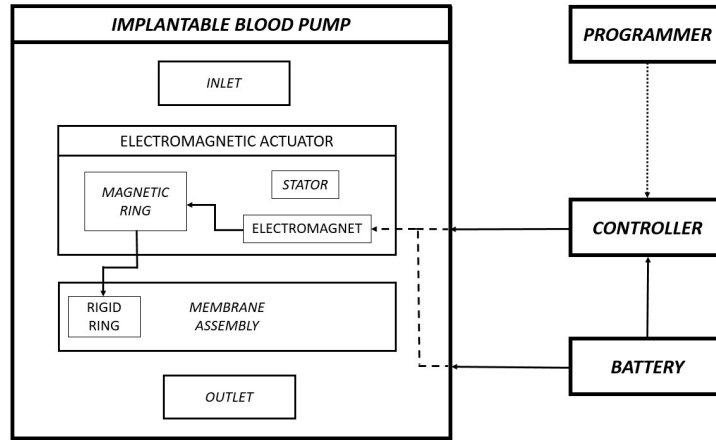
Figure 2: Functional block scheme of the subcomponents of the implantable LVAD pump system as described in [69].

rection of the outlet channel. Therefore, this progressive wave propagation along the membrane transports the blood that is enclosed in the spaces between the membrane wave and the pump head flanges radially inward towards the outlet channel. These masses of blood transported by the membrane wave are referred to as *fluid pockets*. During its wave motion, the membrane may approach to the pump flanges very closely, resulting in a *quasi-contact* configuration that allows to isolate the fluid pockets and to minimize any potential backflow from the outlet towards the inlet, thus increasing the pump efficiency. Moreover, the membrane displacement gets damped by the effect of the surrounding viscous fluid, provoking an energy transfer to the blood that ends up in the form of pressure buildup and addition of kinetic energy. The characteristics of the pressure gradient and the blood flow depend on the size and the shape of the membrane, the spacing between the pump head flanges, and the excitation parameters. Thus, the pump works as an energy transducer, that converts electromechanical energy into hydraulic power.

The pump model of our study is similar to the discoidal design described in Perschall et al. [49], but there are important differences: (i) in the prototype in Perschall's work we find two inlet channels located 180 degrees apart, while in our case we have a unique inlet, that results in a more homogeneous flow field; (ii) our pump actuator is magnetic, not mechanic, so that we avoid the need of contact seals or bearings.

The pump device is coupled with an external controller, that sets the oscillation frequency and voltage applied to the coils in the actuator, and a set of extracorporeal batteries, to power the system. An external programmer is used to configure the working parameters of the pump. A scheme of the complete structure of the LVAD system is represented at Figure 2 .
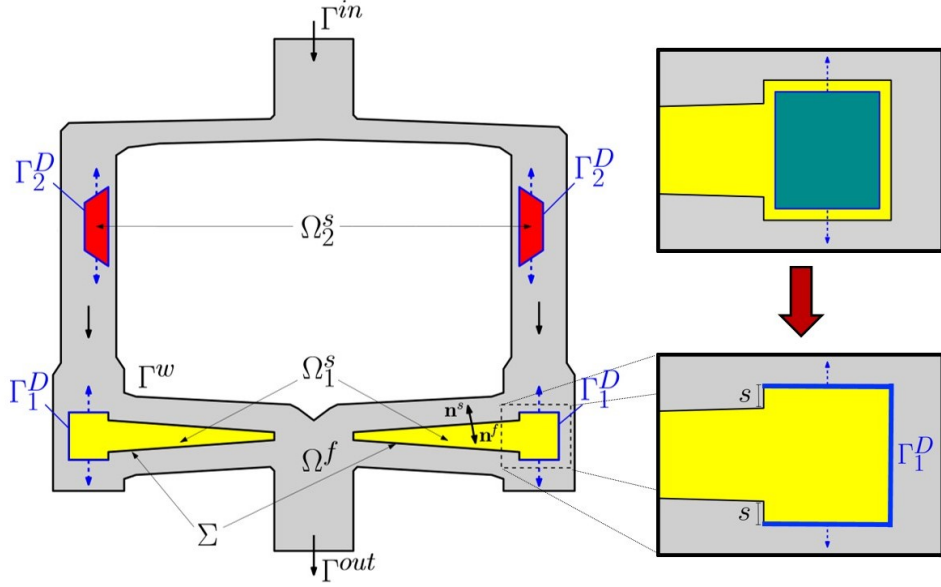
Figure 3: Mathematical and computational domain of interest.

3 Mathematical and numerical methods

3.1 Mathematical model

In this section, we describe the mathematical approach employed to model the interaction between the blood and the oscillating structure in the progressive wave blood pump.

Let Ω be the whole pump domain composed by the region occupied by the fluid and by the immersed oscillating structures. The latter are composed by three main components:

- The *membrane assembly* $\Omega_1^s(t)$ (yellow region in Figures 1, right, and 3, left). It is composed by a flexible region, referred to as the *flexible membrane*, and a rigid region, referred to as the *membrane frame* (see zoom in Figure 3, right). The first region interacts with the fluid through the fluid-structure interface $\Sigma(t)$, where the wave displacement propagates towards the inner orifice of the membrane disc; here no-slip and traction continuity conditions hold true. The second region interacts with the fluid through the interface $\Gamma_1^D(t)$. However, here the motion is not determined by the interaction with the fluid, rather by the movement of the membrane holder (green sub-component in Figure 3, right). For the sake of simplicity, we assume that the movement of the region delimited by Γ_1^D is completely rigid, so that we can apply a displacement field φ directly on Γ_1^D as a Dirichlet condition, see right panel in Figure 3. Accordingly, for the fluid we prescribed a compatible Dirichlet data $\dot{\varphi}$ on Γ_1^D. Notice that, since we

are prescribing two Dirichlet conditions with known data, we cannot say anything about the interface tractions.

- The magnet ring $\Omega_2^s(t)$ (red region in Figures 1, right, and 3). Like the membrane holder, its movement is determined by the pump actuator and thus compatible Dirichlet conditions have been again prescribed at the interface $\Gamma_2^D(t)$ (see Figure 3) both for fluid and structure. Notice that, since the magnet ring is mechanically joined to the membrane holder, the whole complex moves rigidly and therefore the same data $\boldsymbol{\varphi}$ and $\dot{\boldsymbol{\varphi}}$ have been prescribed on the magnet ring.

- The supporting posts (dark blue region in Figure 1). Unlike the magnet ring that surrounds the actuator and thus occupies all the fluid path region, these posts are three thin columns whose presence should not influence significantly blood flow dynamics. For these reason, we decided here to neglect the posts in our domain. In any case, specific investigations on their real influence will be the subject of future studies.

Then, the fluid domain $\Omega^f(t)$ is determined by

$$\Omega^f(t) = \Omega \setminus \Omega^s(t), \tag{1}$$

with $\Omega^s(t) = \Omega_1^s(t) \cup \Omega_2^s(t)$.

The intertwined dynamics arising inside a wave membrane pumps can be mathematically described in the framework of FSI modeling, where a system of partial differential equations describes separately the behaviour of the fluid and of the structure in the respective domains, while proper coupling conditions define their interaction at the interface Σ.

In particular, we assumed the blood to be an incompressible, viscous and Newtonian fluid, because, apart from local (in space and time) exceptions in the *quasi-contact* region, the characteristic size of the pump domain is generally much larger than the diameter of blood cells. Denoting by ρ^f the fluid density and by μ^f the dynamic viscosity, we can then express the fluid Cauchy stress tensor as $\mathbf{T}^f(\mathbf{u}, p) = -p\mathbf{I} + 2\mu^f \mathbf{D}(\mathbf{u})$, with $\mathbf{D}(\mathbf{u}) = \frac{1}{2}(\nabla\mathbf{u} + \nabla\mathbf{u}^T)$, where $\mathbf{u}$ and p are the fluid velocity and pressure, respectively. Therefore, we used the Navier-Stokes equations to model the conservation of momentum and mass of blood, respectively.

Concerning the structural problem, the membrane disc domain Ω_1^s and the magnet ring domain Ω_2^s feature different material properties. In both cases, we considered them to be made of linear and isotropic material, as reported in [49]. To shorten the formulation we have written the structural problem for the whole domain Ω^s with density spatial function $\widetilde{\rho}^s(\mathbf{x}) = \rho_1^s$ if $\mathbf{x} \in \Omega_1^s$ and $\widetilde{\rho}^s(\mathbf{x}) = \rho_2^s$ if $\mathbf{x} \in \Omega_2^s$. Analogous definitions were used for Lamé parameters $\widetilde{\lambda}_s(\mathbf{x})$ and $\widetilde{\mu}^s(\mathbf{x})$. In this way, we could apply Hooke's Law and write the solid Cauchy stress tensor as $\mathbf{T}^s(\mathbf{d}) = \widetilde{\lambda}^s (\nabla \cdot \mathbf{d}) \mathbf{I} + 2\widetilde{\mu}^s \mathbf{D}(\mathbf{d})$, where $\mathbf{d}$ is the structure displacement.

Thus, we have written the elastodynamic equation with respect to the reference configuration $\widehat{\Omega}^s = \Omega^s(0)$ (superscript $\widehat{\cdot}$ has been used to refer to quantities defined in the Lagrangian configuration). We also introduced the first Piola-Kirchhoff tensor $\widehat{\mathbf{T}}^s(\widehat{\mathbf{d}}) = J\,\mathbf{T}^s(\mathbf{d})\mathbf{F}^{-T}$, with $\mathbf{T}^s$ being the solid Cauchy stress tensor, $\mathbf{F} = \nabla\mathbf{x}$ the gradient of deformation and $J = \det\mathbf{F}$ its determinant.

For a given $T > 0$, the fluid-structure interaction problem reads as follows: for each time $t \in (0, T]$, find the fluid velocity $\mathbf{u}(t) : \Omega^f(t) \to \mathbb{R}^3$, the fluid pressure $p(t) : \Omega^f(t) \to \mathbb{R}$, and the structure displacement $\widehat{\mathbf{d}}(t) : \widehat{\Omega}^s \to \mathbb{R}^3$, such that:

$$\rho_f\left(\partial_t\mathbf{u} + \mathbf{u}\cdot\nabla\mathbf{u}\right) - \nabla\cdot\mathbf{T}^f(\mathbf{u}, p) = \mathbf{0} \qquad \text{in } \Omega^f(\mathbf{d}), \tag{2a}$$

$$\nabla\cdot\mathbf{u} = 0 \qquad \text{in } \Omega^f(\mathbf{d}), \tag{2b}$$

$$\widetilde{\rho}_s\partial_{tt}\widehat{\mathbf{d}} - \nabla\cdot\widehat{\mathbf{T}}^s(\widehat{\mathbf{d}}) = \mathbf{0} \qquad \text{in } \widehat{\Omega}^s, \tag{2c}$$

$$\mathbf{u} = \partial_t\mathbf{d} \qquad \text{on } \Sigma(\mathbf{d}), \tag{2d}$$

$$\mathbf{T}^f(\mathbf{u}, p)\,\mathbf{n}^f = -\mathbf{T}^s(\mathbf{d})\,\mathbf{n}^s \qquad \text{on } \Sigma(\mathbf{d}), \tag{2e}$$

where we have highlighted the dependence of the fluid domain Ω^f (and thus of the interface Σ) on the structure displacement $\mathbf{d}$ through its definition (1) (*geometric coupling*).

In System (2), Equations (2a) and (2b) are the non-linear incompressible Navier-Stokes equations, while Equation (2c) is the linear elastodynamic equations. Equations (2d) and (2e) are the coupling conditions imposed on the interface Σ guaranteeing the continuity of velocity and of tractions, respectively, and where $\mathbf{n} = \mathbf{n}^f = -\mathbf{n}^s$ is the external fluid normal. We highlight that the combination of the incompressibility of the fluid (Equation (2b)) with the no-slip kinematic condition (2d) allows to consider a *quasi-contact* assumption when the membrane and the pump walls come into contact. Indeed, previous studies [70, 71] showed that in such conditions, from the mathematical and numerical point of view, contact - strictly speaking - cannot occur when a moving body approaches to a wall, because the interstitial fluid cannot slip away and allow for actual collision. Therefore, despite physical contact may occur between the membrane and the pump head flanges under certain operating conditions of the pump, no contact models were introduced.

Referring to Figure 3, system of equations (2) has to be closed with proper initial and boundary conditions. For the fluid problem, we considered Neumann conditions both at the inlet Γ^{in} and at the outlet Γ^{out} to represent the pressure difference of the pump. Owing to the linearity of the structure problem, we could set the zero level of pressure at the outlet by using homogeneous Neumann condition on Γ^{out}. We also applied an homogeneous Dirichlet condition at the pump walls Γ^w. Finally, in order to model the effect of the actuator on the motion of the membrane frame and the magnet ring, as anticipated we impose

Dirichlet conditions on $\Gamma^D = \Gamma_1^D \cup \Gamma_2^D$. In summary, we have:

$$\mathbf{T}^f(\mathbf{u}, p)\,\mathbf{n}^f = -\Delta P\,\mathbf{n}^f \qquad \text{on } \Gamma^{in}, \tag{3a}$$

$$\mathbf{T}^f(\mathbf{u}, p)\,\mathbf{n}^f = \mathbf{0} \qquad \text{on } \Gamma^{out}, \tag{3b}$$

$$\mathbf{u} = \mathbf{0} \qquad \text{on } \Gamma^w, \tag{3c}$$

$$\mathbf{d} = \boldsymbol{\varphi} \qquad \text{on } \Gamma^D, \tag{3d}$$

$$\mathbf{u} = \dot{\boldsymbol{\varphi}} \qquad \text{on } \Gamma^D, \tag{3e}$$

where $\Delta P > 0$ is a given pressure value corresponding to the pressure difference between the pump outlet and the inlet. At time $t = 0$, we finally imposed the initial conditions $\mathbf{u}(0) = \mathbf{u}_0$, $\mathbf{d}(0) = \mathbf{d}_0$ and $\dot{\mathbf{d}}(0) = \mathbf{w}_0$. In our application, we considered null initial conditions, i.e. $\mathbf{u}_0 = \mathbf{0}$, $\mathbf{d}_0 = \mathbf{0}$ and $\mathbf{w}_0 = \mathbf{0}$.

3.2 Numerical method

3.2.1 The Extended Finite Element Method

Numerical methods for FSI problems are divided into fitted and unfitted methods, depending whether the fluid and solid meshes are fitted to each other or not. In case of fitted methods, the meshes move together. In our problem, fitted methods are not the best option for two main reasons: i) the wave motion of the membrane in the limited pump head region (see Section 2) would cause high distortion of the fluid elements and consequently it would require frequent remeshing; ii) the *quasi-contact* assumption between the membrane and the pump walls would be complex to implement efficiently.

Among the unfitted methods, we selected the Extended Finite Element Method (XFEM), proposed in [64], which is based on the extension of the features of the classical Finite Elements and allows to have higher geometrical flexibility without loss of accuracy. Thanks to such extension, solutions with discontinuities are well described and complex problems with immersed interfaces or structures could be accurately solved. XFEM has proven to be an effective strategy for many problems, in particular for FSI with immersed structures [66, 72, 60, 62], maintaining a good accuracy at the fluid-structure interface. For our study, we specifically refered to the 3D formulation reported in [67], which treats the case of a 3D thin structure, by using a Discontinuous Galerkin (DG) mortaring to weakly impose the continuity conditions (2d)-(2e) at the interface.

Let $\Omega_h^{f,n} \simeq \Omega^f(t^n)$ and $\Omega_h^{s,n} \simeq \Omega^s(t^n)$ be the approximated fluid and structure domains after space (XFEM) and time discretization, the latter being based on the timestep parameter $\Delta t > 0$ such that $t^n = n\Delta t$ for $n = 1, 2, \ldots$.

In the framework of XFEM, a global mesh $\mathcal{T}_h$ defined in Ω_h is kept fixed on the background, while a structure mesh $\mathcal{T}_h^{s,n}$ defined in $\Omega_h^{s,n}$ moves on the foreground cutting the underlying elements. Hence, these elements are overlapped (partially or totally) by the structure mesh and they are divided in multiple subportions that are, in general, polyhedra. Such elements are named *fluid cut ele-*
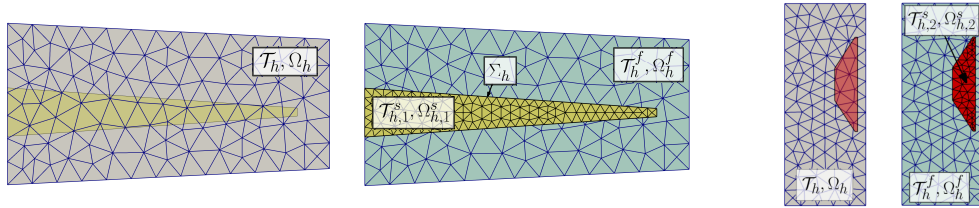
Figure 4: Global mesh $\mathcal{T}_h$ (gray) is overlapped by the structure meshes $\mathcal{T}_{h,1}^s$ (membrane assembly, in yellow) and $\mathcal{T}_{h,2}^s$ (magnet ring, in red). Fluid cut mesh $\mathcal{T}_h^f$ in light blue.

ments. Therefore, we can define the *cut-mesh* as the polyhedral fluid mesh $\mathcal{T}_h^{f,n}$ that covers the fluid domain $\Omega_h^{f,n}$, composed by the union of all fluid elements in $\mathcal{T}_h$ that are not cut by the structure mesh and all the non-overlapped parts of the cut elements. In our case, referring to Figure 4, we have $\mathcal{T}_h^{s,n} = \mathcal{T}_{h,1}^{s,n} \cup \mathcal{T}_{h,2}^{s,n}$, where $\mathcal{T}_{h,i}^{s,n}$, $i = 1, 2$, represent the meshes corresponding to $\Omega_{h,i}^{s,n}$, $i = 1, 2$, that is the membrane assembly ($i = 1$) and the magnet ring ($i = 2$).

Notice that the cut-mesh has to be updated at each time instant, computing the new mesh intersections generated by the motion of the structure mesh. To this aim, we have used the *alternating digital tree* algorithm, see [73].

If the cut elements are separated by the structure in multiple disjoint fluid sub-elements, they are called *split elements* (see Figure 5). In XFEM, the classical Finite Elements Lagrangian basis functions defined on the split element are used to build the numerical solution in all the sub-elements, thus requiring the duplication of the original d.o.f. for each sub-elements (see Figure 5, right). This allows to have an accurate description of the fluid solution across the structure mesh, possibly characterized by discontinuities [62]. For more details on the computational implementation of XFEM in our scenario, we refer the reader to [67].

3.2.2 Full discretization

As mentioned, for the spatial discretization we considered a DG method in the XFEM framework to manage the numerical solution at the fluid-structure interface Σ_h.

Regarding the fluid problem, we needed to consider again a DG approach to ensure continuity of velocity and tractions between two adjacent fluid mesh elements, where at least one of the two is a cut element and thus, possibly, a general polyhedron. Indeed, in this scenario, strong continuity with standard Finite Elements is very hard to implement. This happens close to the interfaces Σ_h and Γ_h^D. For simplicity, we decided to use DG in all of the fluid domain, including far from the interfaces Σ_h and Γ_h^D.

For the structure problem instead, the mesh is always composed of the original tetrahedra, thus standard Finite Elements are considered for its approxima-
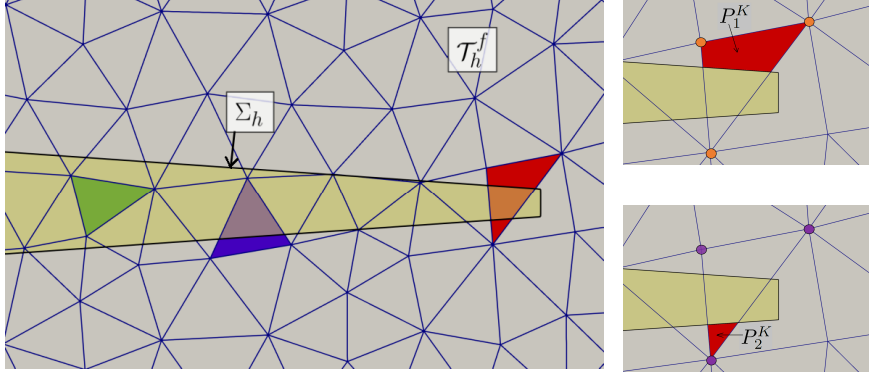
11

Figure 5: Left: Different fluid elements in XFEM: completely overlapped element (green), partially overlapped cut element (blue) and split element (red). Right: D.o.f. duplication of the split element. The same basis functions are used for P_1^K and P_2^K.

tion.

According to the previous discussion, we introduce the following discrete spaces in the fluid and structure domains:

$$X_h^{f,n} = \left\{ v_h \in L^2(\Omega_h^{f,n}) : v_h|_K \in \mathbb{P}_1(K), \forall K \in \mathcal{T}_h \right\},$$

$$X_{h,i}^s = \left\{ \widehat{v}_h \in C^0(\widehat{\Omega}_{h,i}^s) : \widehat{v}_h|_K \in \mathbb{P}_1(K), \forall K \in \widehat{\mathcal{T}}_{h,i}^s \right\} \quad \text{for } i = 1, 2,$$

$$X_h^s = X_{h,1}^s \oplus X_{h,2}^s,$$

and the corresponding spaces for the approximation of fluid velocity and pressure and of structure displacement:

$$\mathbf{V}_{h,\varphi}^n = \left\{ \mathbf{v}_h \in [X_h^{f,n}]^3 : \mathbf{v}_h = \mathbf{0} \text{ on } \Gamma_h^{w,n}, \mathbf{v}_h = \boldsymbol{\varphi} \text{ on } \Gamma_h^{D,n} \right\},$$

$$Q_h^n = X_h^{f,n},$$

$$\mathbf{W}_{h,\varphi} = \left\{ \widehat{\mathbf{w}}_h \in [X_h^s]^3 : \widehat{\mathbf{w}}_h = \widehat{\boldsymbol{\varphi}} \text{ on } \widehat{\Gamma}_h^D \right\}.$$

In view of the DG formulation for the fluid problem, we introduce the mean operator $\{\cdot\}$ and the jump operator $[\![\cdot]\!]$, defined over an element face F as:

$$\{q\} = \frac{1}{2}(q_+ + q_-) \qquad [\![q]\!] = q_+ - q_-,$$

where q is a function that assumes values q_+ and q_- on the two sides of face F.

To manage the geometric non-linearity, we considered an explicit treatment of the geometric coupling by taking the first order extrapolation from the previous timestep, i.e. $\Omega_h^{f,n+1} \simeq \Omega_h^{f,n} = \Omega_h^f(\mathbf{d}_h^n)$. To simplify the notation, we omit in what follows the current temporal index $n+1$ for variables and domains. We

considered the Backward Differentiation Formula of order 1 for the discretization of both the fluid and solid time derivatives and we used a semi-implicit approach for the treatment of the fluid convective term. Let $(\cdot, \cdot)_\Theta$ be the internal product in L^2 in a domain Θ.

Then, we define the following forms:

- The fluid form

$$
\begin{aligned}
\mathcal{A}_h^f(\mathbf{u}_h, \mathbf{u}_h^*, p_h; \mathbf{v}_h, q_h) = & \frac{\rho^f}{\Delta t}\ (\mathbf{u}_h, \mathbf{v}_h)_{\Omega_h^{f,n}} + \rho^f\ (\mathbf{u}_h^* \cdot \nabla \mathbf{u}_h, \mathbf{v}_h)_{\Omega_h^{f,n}} \\
& + 2\mu^f\ (\mathbf{D}(\mathbf{u}_h), \mathbf{D}(\mathbf{v}_h))_{\Omega_h^{f,n}} - (p_h, \nabla \cdot \mathbf{v}_h)_{\Omega_h^{f,n}} + (q_h, \nabla \cdot \mathbf{u}_h)_{\Omega_h^{f,n}} \\
& + \mathbf{c}_h(\mathbf{u}_h^*, \mathbf{u}_h; \mathbf{v}_h) + \mathbf{s}_h(\mathbf{u}_h, p_h; \mathbf{v}_h, q_h) + \mathbf{g}_h(\mathbf{u}_h; \mathbf{v}_h),
\end{aligned}
$$

which collects the terms of the weak formulation of the stabilized Navier-Stokes equations with convective velocity $\mathbf{u}_h^* = \mathbf{u}_h^n$.

In the previous form, we have considered the correction term of the convective term defined as

$$
\begin{aligned}
\mathbf{c}_h(\mathbf{u}_h^*, \mathbf{u}_h; \mathbf{v}_h) = & \frac{\rho^f}{2}\ ((\nabla \cdot \mathbf{u}_h^*)\, \mathbf{u}_h, \mathbf{v}_h)_{\Omega_h^{f,n}} - \sum_{F \in \mathcal{F}_h^{p,n}} \rho^f\ (\{\mathbf{u}_h^*\} \cdot \mathbf{n} [\![\mathbf{u}_h]\!], \{\mathbf{v}_h\})_F \\
& - \sum_{F \in \mathcal{F}_h^{p,n}} \frac{\rho^f}{2}\ ([\![\mathbf{u}_h^*]\!] \cdot \mathbf{n}\ \{\mathbf{u}_h \cdot \mathbf{v}_h\})_F\,,
\end{aligned}
$$

where $\mathcal{F}_h^{p,n}$ is the set of the faces of the fluid mesh elements at time n, excluding the portions overlapped by the structure mesh, see [74, 75].

The stabilization term $\mathbf{s}_h(\mathbf{u}_h, p_h; \mathbf{v}_h, q_h)$ corresponds to the *Continuous Interior Penalty* (CIP) stabilization [76], introduced to handle spurious instabilities due to equal order of Finite Elements for velocity and pressure, and have better control on the convective term and on the incompressibility condition. It is defined over the set $\mathcal{F}_h^n$ of all the faces of the fluid elements at time n as

$$
\begin{aligned}
\mathbf{s}_h(\mathbf{u}_h, p_h; \mathbf{v}_h, q_h) = & \gamma_{v1} \sum_{F \in \mathcal{F}_h^n} \xi\,(Re_F)\, h_F^2\, \|\mathbf{u}_h^* \cdot \mathbf{n}\|_{\infty,F}\, ([\![\nabla \mathbf{u}_h \cdot \mathbf{n}]\!], [\![\nabla \mathbf{v}_h \cdot \mathbf{n}]\!])_F \\
& + \gamma_{v2} \sum_{F \in \mathcal{F}_h^n} \xi\,(Re_F)\, h_F^2 \|\mathbf{u}_h^*\|_{\infty,F}\, ([\![\nabla \cdot \mathbf{u}_h]\!], [\![\nabla \cdot \mathbf{v}_h]\!])_F \\
& + \gamma_p \sum_{F \in \mathcal{F}_h^n} \xi\,(Re_F)\, \frac{h_F^2}{\|\mathbf{u}_h^*\|_{\infty,F}}\, ([\![\nabla p_h]\!], [\![\nabla q_h]\!])_F\,,
\end{aligned}
$$

where γ_{v1}, γ_{v2} and γ_p are positive penalty parameters, Re_F is the local Reynolds number over the face F, h_F is a characteristic mesh size for F, and $\xi(x) = \min(1, x)$.

The ghost-penalty stabilization $\mathbf{g}_h(\mathbf{u}_h; \mathbf{v}_h)$ [77] is added to prevent possible instabilities caused by the arbitrarily small dimension of the generated cut elements. It is defined over the set of faces $\mathcal{F}_h^{\Sigma,n}$ crossed by the interface Σ_h^n as

$$\mathbf{g}_h(\mathbf{u}_h; \mathbf{v}_h) = \gamma_g \sum_{F \in \mathcal{F}_h^{\Sigma,n}} \mu^f h_F \left([\![\nabla \mathbf{u}_h]\!]\mathbf{n}^F, [\![\nabla \mathbf{v}_h]\!]\mathbf{n}^F \right)_F,$$

with $\gamma_g > 0$;

- The form related to the DG fluid terms over the faces in $\mathcal{F}_h^p$, defined as

$$\mathcal{D}_h^f(\mathbf{u}_h, p_h; \mathbf{v}_h, q_h) = -\sum_{F \in \mathcal{F}_h^{p,n}} \left(\left\{ \mathbf{T}^f(\mathbf{u}_h, p_h) \right\} \mathbf{n}^f, [\![\mathbf{v}_h]\!] \right)_F - \sum_{F \in \mathcal{F}_h^{p,n}} \left([\![\mathbf{u}_h]\!], \left\{ \mathbf{T}^f(\mathbf{v}_h, -q_h) \right\} \mathbf{n}^f \right)_F$$
$$+ \sum_{F \in \mathcal{F}_h^{p,n}} \frac{\gamma_{dg} \mu^f}{h_F} \left([\![\mathbf{u}_h]\!], [\![\mathbf{v}_h]\!] \right)_F,$$

where $\gamma_{dg} > 0$ is the stability parameter [78];

- The structure bilinear form

$$\mathcal{A}_h^s \left(\widehat{\mathbf{d}}_h; \widehat{\mathbf{w}}_h \right) = \frac{1}{\Delta t^2} \left(\widetilde{\rho}^s \widehat{\mathbf{d}}_h, \widehat{\mathbf{w}}_h \right)_{\widehat{\Omega}_h^s} + \left(\widetilde{\lambda}^s \nabla \cdot \widehat{\mathbf{d}}_h, \nabla \cdot \widehat{\mathbf{w}}_h \right)_{\widehat{\Omega}_h^s} + 2 \left(\widetilde{\mu}^s \mathbf{D}(\widehat{\mathbf{d}}_h), \mathbf{D}(\widehat{\mathbf{w}}_h) \right)_{\widehat{\Omega}_h^s};$$

- The form $\mathcal{I}_h(\mathbf{u}_h, p_h, \mathbf{d}_h; \mathbf{v}_h, q_h, \mathbf{w}_h)$ corresponding to the DG FSI coupling terms at the fluid-structure interface Σ_h^n [60, 67]:

$$\mathcal{I}_h(\mathbf{u}_h, p_h, \mathbf{d}_h; \mathbf{v}_h, q_h, \mathbf{w}_h) = - \left(\mathbf{T}^f(\mathbf{u}_h, p_h)\mathbf{n}^f, \mathbf{v}_h - \mathbf{w}_h \right)_{\Sigma_h^n} - \left(\mathbf{T}^f(\mathbf{v}_h, q_h)\mathbf{n}^f, \mathbf{u}_h - \frac{\mathbf{d}_h}{\Delta t} \right)_{\Sigma_h^n}$$
$$+ \frac{\gamma_\Sigma \mu^f}{h} \left(\mathbf{u}_h - \frac{\mathbf{d}_h}{\Delta t}, \mathbf{v}_h - \mathbf{w}_h \right)_{\Sigma_h^n},$$

where $\gamma_\Sigma > 0$ is the penalty parameter associated with the interface Σ;

- The form related to the right hand side formed by the terms arising from time integration and Neumann boundary conditions:

$$\mathcal{F}_h(\mathbf{v}_h, q_h, \mathbf{w}_h) = \frac{\rho^f}{\Delta t} (\mathbf{u}_h^n, \mathbf{v}_h)_{\Omega_h^{f,n}} + \sum_{F \in \Gamma^{in}} \left(\Delta P \, \mathbf{n}^f, \mathbf{v}_h \right)_F + \frac{1}{\Delta t^2} \left(\widetilde{\rho}^s \left(2\widehat{\mathbf{d}}_h^n - \widehat{\mathbf{d}}_h^{n-1} \right), \widehat{\mathbf{w}}_h \right)_{\widehat{\Omega}_h^s}$$
$$+ \left(\mathbf{T}^f(\mathbf{v}_h, q_h)\mathbf{n}^f, \frac{\mathbf{d}_h^n}{\Delta t} \right)_{\Sigma_h^n} - \frac{\gamma_\Sigma \mu^f}{h} \left(\frac{\mathbf{d}_h^n}{\Delta t}, \mathbf{v}_h - \mathbf{w}_h \right)_{\Sigma_h^n}.$$

14

The full discretization of problem (2)-(3) reads then as follows: for $n = 0, 1, \ldots$, find $(\mathbf{u}_h, p_h, \mathbf{d}_h) \in \mathbf{V}_{h,\dot{\varphi}} \times Q_h \times \mathbf{W}_{h,\varphi}$ such that $\mathbf{u}_h^0 = \mathbf{0}$, $\mathbf{d}_h^0 = \mathbf{0}$, $\mathbf{d}_h^{-1} = \mathbf{0}$ and

$$\mathcal{A}_h^f(\mathbf{u}_h, \mathbf{u}_h^n, p_h; \mathbf{v}_h, q_h) + \mathcal{A}_h^s\left(\widehat{\mathbf{d}}_h; \widehat{\mathbf{w}}_h\right) + \mathcal{D}_h^f(\mathbf{u}_h, p_h; \mathbf{v}_h, q_h)$$
$$+ \mathcal{I}_h(\mathbf{u}_h, p_h, \mathbf{d}_h; \mathbf{v}_h, q_h, \mathbf{w}_h) = \mathcal{F}_h(\mathbf{v}_h, q_h, \mathbf{w}_h) \quad (4)$$

$$\forall (\mathbf{v}_h, q_h, \mathbf{w}_h) \in \mathbf{V}_{h,0} \times Q_h \times \mathbf{W}_{h,0}.$$

4 Numerical results

In this section, we report 3D numerical results obtained by solving problem (4) for different working conditions of the pump system. The numerical settings and the physical parameters used for our numerical experiments are detailed in Section 4.1. Next, we studied the fluid dynamics induced by the membrane wave deformation in Section 4.2, whereas in Section 4.3 we compared the simulation results for different pressure conditions and we validated the model against experimental data.

4.1 Numerical settings and parameters

In all the numerical experiments, we studied the pump system in continuous conditions, i.e. for fixed pressure and pump working conditions. Therefore, we applied a constant pressure difference ΔP between outlet Γ^{out} and inlet Γ^{in} and an oscillatory motion to the membrane frame (Γ_1^D) and the magnet ring (Γ_2^D).

Boundary conditions (3a)-(3b) define the pressure difference $\Delta P = P^{out} - P^{in} > 0$ acting over the pump, indicating the hydraulic resistance that the wave membrane has to overcome in order to generate positive blood flow in the outlet direction against negative pressure gradients. We studied the pump dynamics for different values of pressure parameter ΔP.

Moreover, we modeled the motion imposed on the magnet ring and on the membrane frame by the electromagnetic actuator by means of the Dirichlet condition (3d). Although in the real pump system the control on the oscillations may not be optimal due to instabilities in the electro-mechanical dynamics or manufacturing tolerances, its motion can be approximated with a sinusoid in time in the vertical direction. Therefore, in our simulation the displacement function φ has been defined as

$$\varphi(t) = \frac{\Phi}{2} \sin(2\pi f t) \mathbf{e}_z \qquad t \in (0, T), \quad (5)$$

where f is the excitation frequency of the structure and Φ is the so-called *stroke* parameter. Thus, the pair (f, Φ) defines the *operating point* of the wave membrane. In all our simulations, we have set $f = 120$ Hz, and $\Phi = 1.06$ mm, which are values of interest for real applications of the pump device [69].
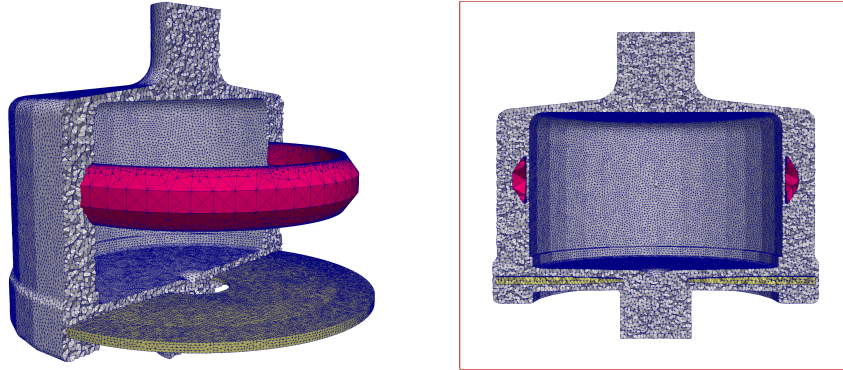
Figure 6: Prospective visualization and section of the fluid mesh $\mathcal{T}_h^f$ (gray), the membrane $\mathcal{T}_h^{s,1}$ (yellow) and magnet mesh $\mathcal{T}_h^{s,2}$ (red).

The unfitted fluid and the solid meshes used for the simulations have been shown in Figure 6. The background mesh $\mathcal{T}_h$ has $1.2M$ elements, while the membrane mesh $\mathcal{T}_{h,1}^s$ and the magnet ring mesh $\mathcal{T}_{h,2}^s$ have $280k$ and $50k$ elements, respectively. These meshes showed positive convergence results with respect to solutions computed on finer meshes. Notice that we have removed from the membrane computational domain the step before the membrane frame (i.e., we take $s = 0$ with respect to Figure 3, right) in order to obtain a smooth membrane surface. Concerning the temporal discretization of the simulation interval $(0, T)$, we need to choose a timestep that is sufficiently small to capture the effect of membrane wave propagation on the flow dynamics. Therefore, given the high frequency of membrane vibration, we took $\Delta t = 0.2$ ms, corresponding to less than $1/40$ of the period of oscillation, which is $\tau = 8.33$ ms. The values of the physical parameters of the pump system have been reported in Table 1. We remind that the Lamé's parameters used in Section 3 can be derived as $\lambda_i^s = E_i^s \nu_i^s / (1+\nu_i^s)(1-2\nu_i^s)$ and $\mu_i^s = E_i^s / 2(1+\nu_i^s)$, for $i = 1, 2$.

Physical parameter	Value	Unit
ρ^f : Blood mass density	1	$[g/cm^3]$
μ^f : Blood dynamic viscosity	0.035	$[(dyne/cm^2) \cdot s]$
ρ_1^s : Membrane mass density	1.125	$[g/cm^3]$
E_1^s : Membrane Young's modulus	$1.686 \cdot 10^7$	$[dyne/cm^2]$
ν_1^s : Membrane Poisson's ratio	0.49	
ρ_2^s : Magnet mass density	7.85	$[g/cm^3]$
E_2^s : Magnet Young's modulus	$2.05 \cdot 10^{12}$	$[dyne/cm^2]$
ν_2^s : Magnet Poisson's ratio	0.28	

Table 1: Values of the physical parameters of the main components of the pump system used in the numerical experiments.

The linear system obtained at each timestep after the XFEM-based discretization has been solved with a monolythic approach with a GMRES solver preconditioned by a block Gauss-Seidel preconditioner. The problem has been solved in the C++ finite element LIFEV library (www.lifev.org) in a multi-thread parallel environment.

4.2 Flow analysis and membrane deformation

We simulated the pump system in continuous conditions with $T = 25$ ms (that is equivalent to 3 complete oscillations of magnet ring and membrane frame) with pressure gradient $\Delta P = 50$ mmHg. The penalty parameters used for this simulation were: $\gamma_\Sigma = 10^6$, $\gamma_{dg} = 10^3$, $\gamma_{v1} = 5 \cdot 10^{-2}$, $\gamma_{v2} = 5 \cdot 10^{-1}$, $\gamma_p = 5 \cdot 10^{-2}$ and $\gamma_g = 1$.

The numerical results of the simulation have been represented in Figure 7, where the vertical displacement of the flexible membrane, the fluid velocity (left panel) and pressure (right panel) fields are shown in a cross-sectional view of the pump domain at time $t = 18.8$ ms, corresponding to the maximum point of the membrane frame displacement during the third oscillation. Such results confirm that the propelling action of the wave membrane succeeds in generating positive outflow, despite the adverse pressure difference existing between the endings of the pump domain. In particular, referring to the right panel of Figure 7, we can identify three sub-regions in the pressure field: i) a low-pressure area (region A), extending from the inlet down to the membrane frame; ii) a high-pressure area (region B), in proximity to the outlet channel; and the so-called *fluid pocket* (region C), consisting of the fluid portion enclosed between the wave membrane and the pump head flange. The propagation of the fluid pockets in the pump head is at the core of wave pumping mechanism: indeed, by means of the progressive wave, the membrane actively transports the fluid pocket from region A to region B, going against the pressure gradient. In addition, by looking at the pressure field in the remaining part of the pump domain, outside the pump head region, we can see that the pressure gradient favors blood propulsion through the pump: specifically, in region A, blood flows from the inlet (green) down to the membrane frame (blue); while, in region B, it is propelled from the membrane tip (red) to the outlet channel (orange).

The success of the wave membrane pumping technology is also confirmed by the analysis of the volume balance reported in Figure 8, left, where we showed the evolution in time of the volumes V_{in} and V_{out}, representing the volumes of blood entering in and exiting from the pump domain, respectively. These volume quantities were computed integrating the corresponding volumetric flow rate using the trapezoidal rule. Hence, we have $V_\beta^n = \frac{\Delta t}{2}(Q_\beta^n + Q_\beta^{n-1})$, $\beta = \{in, out\}$, where Q_{in} and Q_{out} are the computed pump inflow and outflow rates, respectively. Notice that, after a short interval of adaptation, the two curves V_{in} and V_{out} start oscillating with the same period of the membrane vibrations. Since the values of the divergence of the velocity are very small ($\|\nabla \cdot \mathbf{u}\| <$
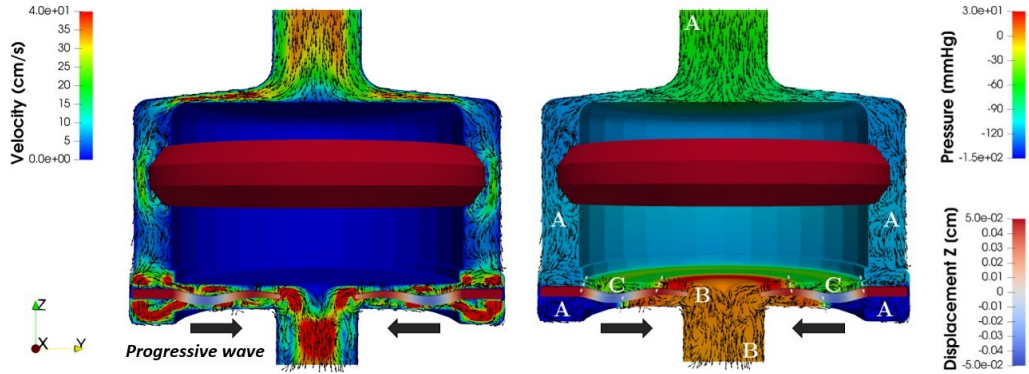
Figure 7: Vertical slice visualization of the three-dimensional flexible membrane vertical displacement, fluid velocity (left) and pressure (right) fields in the full pump domain at time $t = 18.8$ ms.
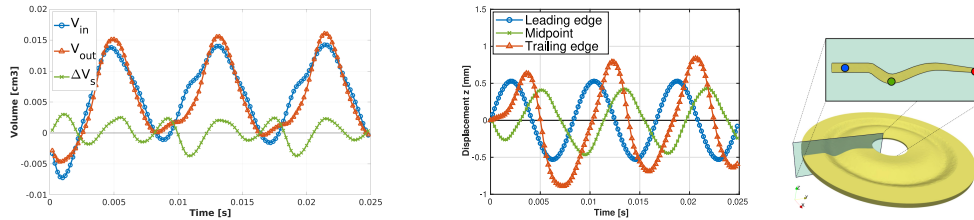

Figure 8: Left: Volume conservation through time. Middle: Vertical displacement of three points of the membrane through time. Right: The three points of the membrane section: the leading edge (blue), the trailing edge (red) and a midpoint in between (green).

$3 \cdot 10^{-4} \, 1/s$), the small discrepancy between V_{in} and V_{out} is due to the slight incremental variation of the membrane volume $\Delta V_s^n = |\Omega_{h,1}^{s,n}| - |\Omega_{h,1}^{s,n-1}|$, with $\Omega_{h,1}^s$ the discretized membrane domain. Indeed, we have $V_{out}^n - V_{in}^n \simeq \Delta V_s^n$ for all n. Since the magnet ring is a rigid structure, it was not considered in the volume balance. Notice that the observed variation of the membrane volume corresponds to a relative change of less than 2‰ of the membrane volume. This small variation is explained by the not completely incompressibility of the membrane ($\nu_1^s = 0.49$) and by the numerical approximation. Anyway, we verified that such volume variation decreases when the mesh size h is reduced.

We also studied the displacement in time of three key points of the membrane section (see Figure 8, middle): the leading edge (blue), extracted from the membrane frame, the trailing edge (red), in correspondence to the membrane tip, and a third point in-between in the membrane section (green), see Figure 8, right. Since the motion of the membrane frame is governed by (5), the leading edge oscillates between -0.53 mm and 0.53 mm with an excitation frequency equal to 120 Hz. The displacement curves of the midpoint and the

trailing edge also become periodic, with the same frequency of the leading edge. In particular, we can notice that the midpoint shows an oscillation amplitude that is smaller than the one of the leading edge, that is likely due to the damping effect of the surrounding viscous fluid on the membrane motion. However, the trailing edge actually is the point that undergoes to the highest displacement, because the most internal portion of the membrane is thinner and therefore it offers less inertial resistance to the wave elastic motion. In fact, the cross-section of the membrane is designed to make the membrane tip reach the quasi-contact configuration with the pump head flanges, allowing for the isolation of the fluid pockets and for the blockage of possible backflows. Nonetheless, the trailing edge never reaches the collision point with the pump flanges in our simulations, in agreement with the theoretical results reported in [70, 71].

Next, we studied more in detail the effect of the wave propagation on the flow dynamics during the whole cycle of membrane oscillation. To this aim, in Figure 9, we analyzed the dynamics in the pump head region for four different time instants in the third period of oscillation of the membrane frame, showing for each time point the radial velocity of the flexible membrane, the blood velocity (left) and pressure (right) fields.

- In Figure 9a, the membrane frame has returned back to its initial position coming from below. During this upwards vertical displacement, part of the blood coming from the inlet flows above the membrane wave, leading to the formation of an upper fluid pocket (Pocket A), while the remaining part is gathered in the low pressure area below the membrane frame. Meanwhile, in the most internal part of the pump head, another fluid pocket (Pocket B) below the membrane is transported towards the outlet channel thanks to the progressive propagation of the membrane wave. Notice that the simultaneous propagation of two fluid pockets is made possible by the high frequency of oscillation that introduces a second mode of deformation in the elastic membrane. We can also notice some recirculation areas nearby the membrane frame and in proximity to the membrane tip, caused by the flapping motion of the membrane [79].

- When the membrane frame reaches the maximum point of the oscillation (time $t = 18.8$ ms), the formation of the upper fluid pocket (Pocket A) is completed and the blood below the membrane frame reaches its maximum point of accumulation (see Figure 9b). While the membrane tip is raising to reduce potential backflows, we can observe a local increase of the pressure in that area that contributes to the blood propulsion towards the outlet. Nonetheless, the ongoing vortex dynamics below the trailing edge of the membrane seems to hamper the full release of the lower fluid pocket (Pocket B) in the outlet channel, penalizing the overall outflow.

- As the membrane frame moves downwards (Figure 9c), it compresses the fluid accumulated in the area below during the ascending phase. This
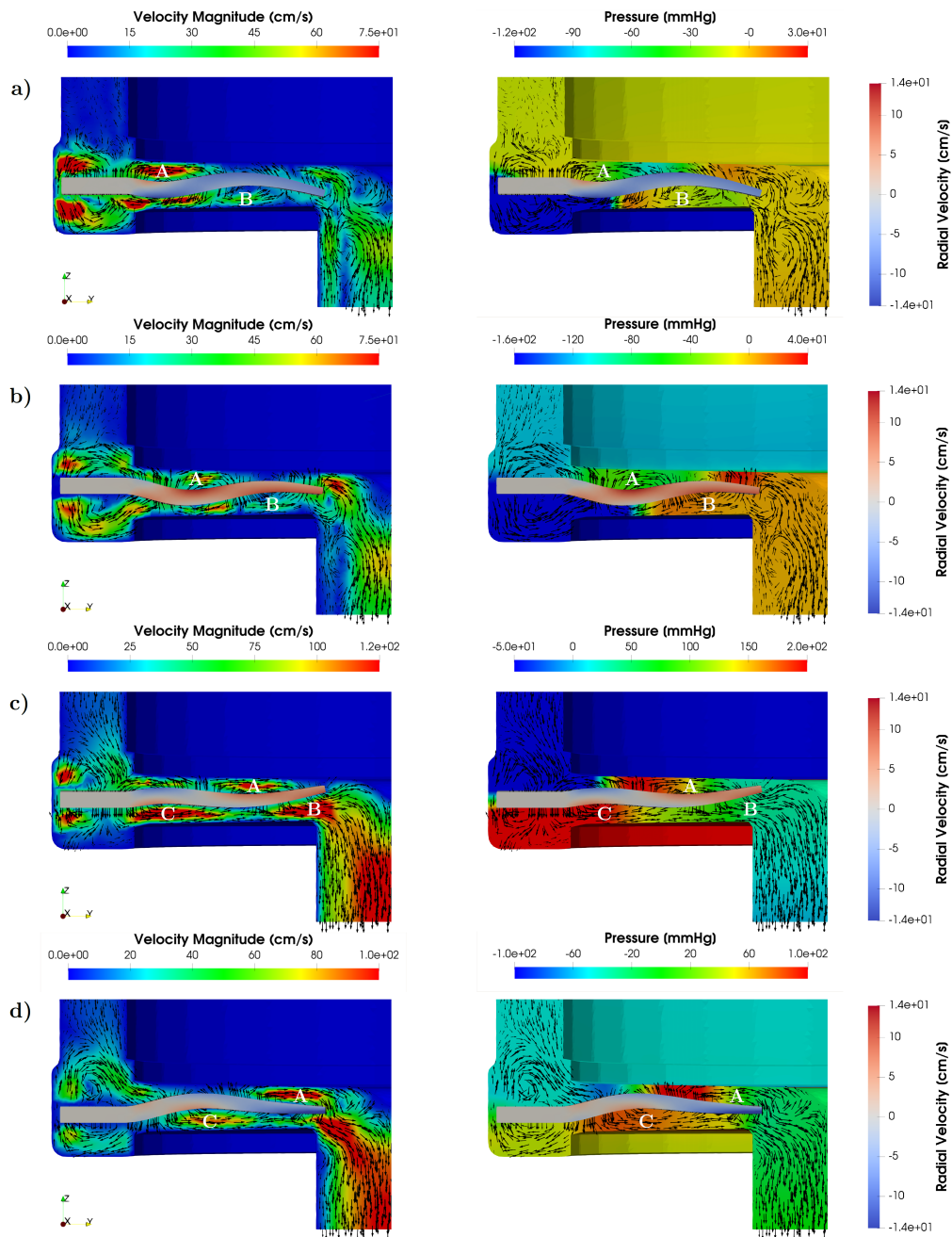
Figure 9: Visualization of the velocity field (left) and of the pressure field (right) in a vertical section of the pump head region for four different time istants: a) $t = 16.6$ ms, b) $t = 18.8$ ms, c) $t = 20.8$ ms, and d) $t = 22.8$ ms. Capital letters A, B and C indicate the fluid pockets, getting formed and transported by wave propagation.

causes a drastic increase of the pressure below the membrane, that strongly propels the blood in the outlet direction, contributing to the formation of a new lower fluid pocket (Pocket C). Above the flexible membrane, the upper fluid pocket (Pocket A) proceeds in its radial propagation and the tip of the membrane has reached its quasi-contact configuration with the superior pump flange. We can observe that the velocity values around the quasi-contact region are very low, indicating that potential backflows are blocked or minimized. Moreover, the upper quasi-contact configuration allows to achieve the point of maximum delivery of the fluid pocket below (Pocket B). The combination of these phenomena results in successful pumping dynamics and in rapid increase of the blood outflow.

- Then, the membrane frame reaches the minimum point of its oscillation, completing the formation of the new fluid pocket (Pocket C) below the flexible membrane, see Figure 9d. Furthermore, blood from the upper pocket (Pocket A) is delivered into the outlet channel, and the cycle can restart.

We conclude our analysis of the flow patterns in the blood pump by noticing recirculation regions around the magnet ring (see Figure 7, left) and nearby the outlet section (see Figure 9b, left). This is of utmost importance in view of a clinical analysis of the pump. Indeed, on the one hand, it is well known that recirculation regions may lead to thrombus formation [80, 81]; but, on the other hand, other studies [82, 83] showed that alternating vortices can create a jet effect that may increase pump outflow. Therefore, it is not clear which is the best scenario and these issues need a specific investigation. However, we remark that alternative designs of the CorWave LVAD are in development with the aim to reduce the risk of recirculations and improve hemocompatibility.

4.3   Parametric analysis

In this section we compare the pump performance for different pressure conditions, varying the value of ΔP. In particular we considered $\Delta P \in \{50, 55, 60\}$ mmHg, being these values close to the real applications of the blood pump for partial left ventricle support, where ΔP varies from 0 mmHg during systole (aortic valve open) to 70 mmHg during diastole (aortic valve closed). For this set of simulations, we used $T = 20$ ms. Table 2 reports the values of the penalty parameters used for this set of simulations to ensure stability for each flow regime.

As the pressure difference ΔP acting over the pump between outlet and inlet increases, the hydraulic resistance inside the pump gets higher and as a consequence, for a fixed operating point of the membrane, the pump outflow gets smaller. This is confirmed by the results reported in the left plot of Figure 10, where we see that the amplitude of the outflow volume rate curves is lower when the pressure difference ΔP is larger. Notice that, although in all the cases

	$\Delta P = 50$ mmHg	$\Delta P = 55$ mmHg	$\Delta P = 60$ mmHg
γ_Σ	10^6	10^6	10^6
γ_{dg}	10^3	10^3	10^3
γ_g	1	1	1
γ_{v1}	0.05	0.05	0.5
γ_{v2}	0.5	0.5	5
γ_p	0.05	0.1	0.1

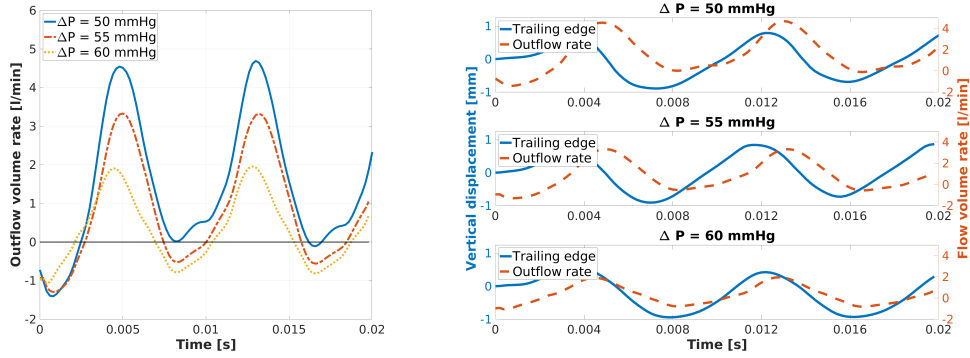Table 2: Penalty stability parameters for different pressure conditions.

Figure 10: Left: Time profile of the outflow volume rate for three different pressure head conditions ΔP. Right: Vertical displacement of the trailing edge (solid line) for each ΔP value, in relation with the outflow volume rate membrane volume (dashed line).

there are time intervals with negative outflow, the average in time of the outflow rate is always positive, as required by the correct functioning of the pump.

Furthermore, in the right panel of Figure 10, we displayed in the same figure the pump outflow rate and the vertical displacement of the trailing edge (corresponding to the membrane tip, as in Figure 8, right). Even though the displacement curve is not significantly affected by the different pressure conditions, we can notice that the trailing edge precedes the outflow curve in all the three cases. Indeed, as discussed in Section 4.2, the trailing edge is strictly related to the isolation and the release of the fluid pockets into the outlet channel. Therefore, its displacement drives the time evolution of the outflow volume rate with a small delay due to the time needed for the propagation of the blood from the fluid pocket throughout the outlet channel.

4.4 Validation against experimental measures

As a conclusion, we report results about the validation of the proposed numerical model. To this aim, we compared our simulation results with experimental measurements obtained when testings the blood pump in the same operating

conditions. In particular, the hydraulic performance of the blood pump is assessed by means of *in vitro* testings perfomed in a pump characterization bench, consisting of a reservoir and tubing in which the hydraulic resistance can be set by adding centrifugal pumps in a series circuit with the CorWave LVAD. This system is equipped with a Wheatstone bridge pressure sensor, to measure the pressure head arisen between the outlet and the inlet of the pump, and with an ultrasonic flowmeter clamped adjacent to the LVAD outlet, to measure the pump outflow volume rate. Therefore, for any given operating point of the wave membrane, we can use such measurements to determine the hydraulic performance of the pump when it is exposed to different pressure conditions depending on the action of the centrifugal pumps.

Specifically, we have at our disposal several measures when the operating membrane point is given by $f = 120$ Hz and $\Phi = 1.06$ mm. Such quantities are given by the average in time of the pressure head P^{data} and the corresponding ouflow rate Q^{data}. The data points are represented in the experimental curve in Figure 11, together with the numerical outflow flow rate Q^{sim} corresponding to the pressure differences $\Delta P \in \{50, 55, 60\}$ mmHg. From this figure, we observe a very good agreement between numerical results and experimental findings.
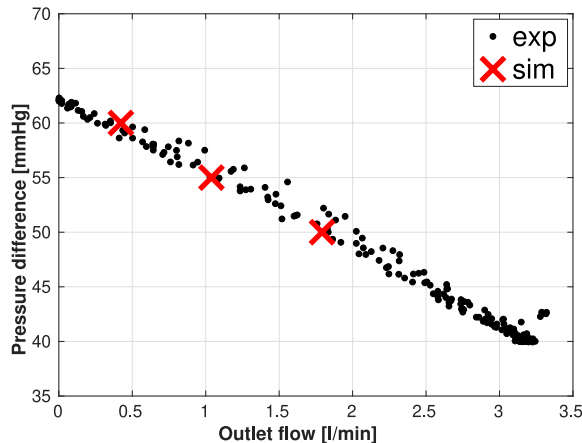

Figure 11: Validation of the model results (red crosses) against the experimental data (black dots).

To quantify the discrepancy, in Table 3 we reported the comparison between the estimated flow rate Q^{sim} with the experimental data Q^{data}, where the latter corresponds to the measurement associated to the data point that minimizes $|P^{data} - \Delta P|$.

These results highlight a very good quantitative agreement with the experimental findings, meaning that the numerical model is able to quantitatively reproduce the pump dynamics with good confidentiality for the analyzed pressure conditions. Indeed, the prediction errors are small for all considered ΔP; in

	$\Delta P = 50$ mmHg	$\Delta P = 55$ mmHg	$\Delta P = 60$ mmHg
Q^{data}	$1.834 \frac{1}{\min}$	$1.091 \frac{1}{\min}$	$0.352 \frac{1}{\min}$
Q^{sim}	$1.792 \frac{1}{\min}$	$1.039 \frac{1}{\min}$	$0.400 \frac{1}{\min}$
$|Q^{data} - Q^{sim}|$	$0.042 \frac{1}{\min}$	$0.052 \frac{1}{\min}$	$0.048 \frac{1}{\min}$

Table 3: Experimental and simulation data for the model validation against experimental mesures.

particular, the relative error is lower than 5% for $\Delta P = 50, 55$ mmHg, that are the working conditions corresponding to higher pump flow support. However, we note that the operating conditions of the pump considered for the model validation do not correspond with those required for the final application of the pump.

5 Conclusions

In this work we numerically studied the novel wave membrane technology employed in progressive wave blood pumps, in view of the optimization of the device performance. To this aim, we simulated the fluid-structure interaction between the membrane and the blood flow in a realistic 3D pump domain using the unfitted XFEM-DG approach. We discussed the effect of the progressive propagation of the membrane on the blood dynamics, highlighting the mechanisms that allow the pump to propel blood against a negative pressure gradient. We also validated our numerical model against experimental measures at different pressure conditions.

We can conclude that our computational model is able to capture with excellent accuracy the behavior of the pump, despite the simplifications underneath its modeling. Therefore, we believe that this and future computational studies represent reliable tools for the prediction of the hydraulic performance of the pump under different working conditions and to support the device design.

The pump and membrane have recently undergone some revisions and improvements, thus, in our future studies, we will use the proposed model to evaluate and optimize the new pump design, examining the performance across a wider range of clinical conditions, including generation of physiologic pulse hemodynamics.

6 Acknowledgements

References

[1] G. Savarese and L. H. Lund. Global public health burden of heart failure. *Cardiac failure review*, 3(1):7, 2017.

[2] C. T. January, L. S. Wann, H. Calkins, L. Y. Chen, J. E. Cigarroa, J. C. Cleveland, Jr, P. T. Ellinor, M. D. Ezekowitz, M. E. Field, K. L. Furie, et al. 2019 AHA/ACC/HRS focused update of the 2014 AHA/ACC/HRS guideline for the management of patients with atrial fibrillation: A report of the American College of Cardiology/American Heart Association task force on clinical practice guidelines and the heart rhythm society in collaboration with the Society of Thoracic Surgeons. *Circulation*, 140(2):e125–e151, 2019.

[3] A. C. Alba and D. H. Delgado. The future is here: ventricular assist devices for the failing heart. *Expert Review of Cardiovascular Therapy*, 7(9):1067–1077, 2009.

[4] C. Bartoli and R. Dowling. The next wave of mechanical circulatory support devices. *Cardiac Interventions Today*, 13(1):53–59, 2019.

[5] W. E. Cohn, D. L. Timms, and O. H. Frazier. Total artificial hearts: past, present, and future. *Nature Reviews Cardiology*, 12(10):609, 2015.

[6] B. P. Griffith, R. L. Kormos, H. S. Borovetz, K. Litwak, J. F. Antaki, V. L. Poirier, and K. C. Butler. HeartMate II left ventricular assist system: from concept to first clinical use. *The Annals of thoracic surgery*, 71(3):S116–S120, 2001.

[7] S. Westaby, A. P. Banning, R. Jarvik, O. H. Frazier, D. W. Pigott, X. Y. Jin, P. A. Catarino, S. Saito, D. Robson, A. Freeland, et al. First permanent implant of the Jarvik 2000 Heart. *The Lancet*, 356(9233):900–903, 2000.

[8] K. Bourque, D. B. Gernes, H. M. Loree, J. S. Richardson, V. L. Poirier, N. Barletta, A. Fleischli, G. Foiera, T. M. Gempp, R. Schoeb, et al. HeartMate III: pump design for a centrifugal LVAD with a magnetically levitated rotor. *ASAIO journal*, 47(4):401–405, 2001.

[9] J. A. LaRose, D. Tamez, M. Ashenuga, and C. Reyes. Design concepts and principle of operation of the heartware ventricular assist system. *Asaio Journal*, 56(4):285–289, 2010.

[10] S. Saito, K. Yamazaki, T. Nishinaka, Y. Ichihara, M. Ono, S. Kyo, T. Nishimura, T. Nakatani, K. Toda, Y. Sawa, et al. Post-approval study of a highly pulsed, low-shear-rate, continuous-flow, left ventricular assist device, evaheart: a japanese multicenter study using j-macs. *The Journal of Heart and Lung Transplantation*, 33(6):599–608, 2014.

[11] A. L. Meyer, C. Kuehn, J. Weidemann, D. Malehsa, C. Bara, S. Fischer, A. Haverich, and M. Strüber. Thrombus formation in a HeartMate II left ventricular assist device. *The Journal of thoracic and cardiovascular surgery*, 135(1):203–204, 2008.

[12] M. Behbahani, M. Behr, M. Hormes, U. Steinseifer, D. Arora, O. Coronado, and M. Pasquali. A review of computational fluid dynamics analysis of blood pumps. *European Journal of Applied Mathematics*, 20(4):363–397, 2009.

[13] F. Castagna, E.J. Stöhr, A. Pinsino, J.R. Cockcroft, J. Willey, A.R. Garan, V.K. Topkara, P.C. Colombo, M. Yuzefpolskaya, and B.J. McDonnell. The unique blood pressures and pulsatility of lvad patients: current challenges and future opportunities. *Current hypertension reports*, 19(10):85, 2017.

[14] C. A. Taylor and C. A. Figueroa. Patient-specific modeling of cardiovascular mechanics. *Annual Review of Biomedical Engineering*, 11:109–134, 2009.

[15] N. P. Smith, D. P. Nickerson, E. J. Crampin, and P. J. Hunter. Multiscale computational modelling of the heart. *Acta Numerica*, 13:371–431, 2004.

[16] P. Colli Franzone, L. F. Pavarino, and S. Scacchi. *Mathematical Cardiac Electrophysiology*. Springer, 2014.

[17] A. Quarteroni, L. Dedè, A. Manzoni, and C. Vergara. *Mathematical Modelling of the Human Cardiovascular System - Data, Numerical Approximation, Clinical Applications*. Cambridge University Press, 2019.

[18] A. Quarteroni and G. Rozza. Optimal control and shape optimization of aorto-coronaric bypass anastomoses. *Mathematical Models and Methods in Applied Sciences*, 13(12):1801–1823, 2003.

[19] T. Lassila, A. Manzoni, A. Quarteroni, and G. Rozza. Boundary control and shape optimization for the robust design of bypass anastomoses under uncertainty. *ESAIM: Mathematical Modelling and Numerical Analysis*, 47(4):1107–1131, 2013.

[20] S. Morganti, N. Brambilla, A. S. Petronio, A. Reali, F. Bedogni, and F. Auricchio. Prediction of patient-specific post-operative outcomes of TAVI procedure: the impact of the positioning strategy on valve performance. *Journal of biomechanics*, 49(12):2513–2519, 2016.

[21] M. Bianchi, G. Marom, R. P. Ghosh, O. M. Rotman, P. Parikh, L. Gruberg, and D. Bluestein. Patient-specific simulation of transcatheter aortic valve replacement: impact of deployment options on paravalvular leakage. *Biomechanics and modeling in mechanobiology*, 18(2):435–451, 2019.

[22] F. Sturla, M. Ronzoni, M. Vitali, A. Dimasi, R. Vismara, G. Preston-Maher, G. Burriesci, E. Votta, and A. Redaelli. Impact of different aortic valve calcification patterns on the outcome of transcatheter aortic valve implantation: a finite element study. *Journal of biomechanics*, 49(12):2520–2530, 2016.

[23] C. Capelli, G. M. Bosi, E. Cerri, J. Nordmeyer, T. Odenwald, P. Bonhoeffer, F. Migliavacca, A. M. Taylor, and S. Schievano. Patient-specific simulations of transcatheter aortic valve stent implantation. *Medical & biological engineering & computing*, 50(2):183–192, 2012.

[24] D. R. Hose, A. J. Narracott, B. Griffiths, S. Mahmood, J. Gunn, D. Sweeney, and P. V. Lawford. A thermal analogy for modelling drug elution from cardiovascular stents. *Computer methods in biomechanics and biomedical engineering*, 7(5):257–264, 2004.

[25] B. Balakrishnan, A. R. Tzafriri, P. Seifert, A. Groothuis, C. Rogers, and E. R. Edelman. Strut position, blood flow, and drug deposition: implications for single and overlapping drug-eluting stents. *Circulation*, 111(22):2958–2965, 2005.

[26] C. Vergara and P. Zunino. Multiscale boundary conditions for drug release from cardiovascular stents. *Multiscale Modeling & Simulation*, 7(2):565–588, 2008.

[27] P. Zunino, C. D'Angelo, L. Petrini, C. Vergara, C. Capelli, and F. Migliavacca. Numerical simulation of drug eluting coronary stents: mechanics, fluid dynamics and drug release. *Computer Methods in Applied Mechanics and Engineering*, 198(45-46):3633–3644, 2009.

[28] B. Ene-Iordache, C. Semperboni, G. Dubini, and A. Remuzzi. Disturbed flow in a patient-specific arteriovenous fistula for hemodialysis: Multidirectional and reciprocating near-wall flow patterns. *J. Biomech.*, 48(10):2195–2200, 2015.

[29] S. Stella, C. Vergara, L. Giovannacci, A. Quarteroni, and G. Prouse. Assessing the disturbed flow and the transition to turbulence in the arteriovenous fistula. *Journal of Biomechanical Engineering*, 141(10):101010, 2019.

[30] D. Papantonis. Numerical prediction of the shear stresses and of the mean stay time for radial flow impellers. In *Proceedings of the International Workshop on Rotary blood pumps*, pages 63–9. 2nd Univ–Dept. of Surgery, 1991.

[31] M. Pinotti and E. S. Rosa. Computational prediction of hemolysis in a centrifugal ventricular assist device. *Artificial Organs*, 19(3):267–273, 1995.

[32] L. Wiegmann, S. Boës, D. De Zélicourt, B. Thamsen, M. S. Daners, M. Meboldt, and V. Kurtcuoglu. Blood pump design variations and their influence on hydraulic performance and indicators of hemocompatibility. *Annals of biomedical engineering*, 46(3):417–428, 2018.

[33] B. Ghadimi, A. Nejat, S. A. Nourbakhsh, and N. Naderi. Shape optimization of a centrifugal blood pump by coupling CFD with metamodel-assisted genetic algorithm. *Journal of Artificial Organs*, 22(1):29–36, 2019.

[34] GM. Liu, DH. Jin, JY. Zhou, Y. Zhang, HB. Chen, H. S. Sun, SS. Hu, and XM. Gui. Numerical investigation of the influence of blade radial gap flow on axial blood pump performance. *Asaio Journal*, 65(1):59–69, 2019.

[35] J. Wu, J. F. Antaki, W. R. Wagner, T. A. Snyder, B. E. Paden, and H. S. Borovetz. Elimination of adverse leakage flow in a miniature pediatric centrifugal blood pump by computational fluid dynamics-based design optimization. *ASAIO journal*, 51 5:636–43, 2005.

[36] J. Wu, J. F. Antaki, G. Bearnson, D. Paden, T. Maher, and B. E. Paden. Hydrodynamic and hemodynamic design improvement of the magnetically levitated HEARTQUEST LVAD. *Asaio Journal*, 52(2):56A, 2006.

[37] K. H. Fraser, M. E. Taskin, T. Zhang, J. S. Richardson, B. Gellman, K. Dasse, B. P. Griffith, and Z. J. Wu. The effect of impeller position on cfd calculations of blood flow in magnetically levitated centrifugal blood pumps. In *Summer Bioengineering Conference*, volume 44038, pages 119–120. American Society of Mechanical Engineers, 2010.

[38] J. Bonnemain, S. Deparis, and A. Quarteroni. Connecting ventricular assist devices to the aorta: a numerical model. In *Imagine Math*, pages 211–224. Springer, 2012.

[39] J. Bonnemain, A. C. I. Malossi, M. Lesinigo, S. Deparis, A. Quarteroni, and L. K. Von Segesser. Numerical simulation of left ventricular assist device implantations: comparing the ascending and the descending aorta cannulations. *Medical engineering & physics*, 35(10):1465–1475, 2013.

[40] R. O. Prather, M. W. Ni, E. Divo, A. J. Kassab, and W. M DeCampli. Pulsatile multiscale fluid-structure interaction modeling for optimal left ventricular assist device implantation. In *ASTFE Digital Library*. Begel House Inc., 2018.

[41] S. J. Sonntag, E. Zebrowski, M. Neidlin, K. Hugenroth, R. Benkowski, T. Motomura, and T. A. S. Kaufmann. Virtual fitting and hemodynamic

simulation of the EVAHEART 2 left ventricular assist device and double-cuff tipless inflow cannula. *ASAIO journal (American Society for Artificial Internal Organs: 1992)*, 2018.

[42] L. Pauli, J. Nam, M. Pasquali, and M. Behr. Transient stress-based and strain-based hemolysis estimation in a simplified blood pump. *International journal for numerical methods in biomedical engineering*, 29(10):1148–1160, 2013.

[43] H. Li, Z. Gou, F. Huang, X. Ruan, W. Qian, and X. Fu. Evaluation of the hemolysis and fluid dynamics of a ventricular assist device under the pulsatile flow condition. *Journal of Hydrodynamics*, pages 1–11, 2018.

[44] K. Gu, Z. Guan, Y. Chang, B. Gao, Y. Ling, Z. Song, and F. Wan. Hemodynamic effects of pulsatile unloading of left ventricular assist devices (lvad) on intraventricular flow and ventricular stress. *Journal of Biomechanics*, page 109425, 2020.

[45] R. Osuna-Orozco, V. K. Chivukula, and A. Aliseda. Numerical modeling of platelet margination and its impact on left ventricular assist device thrombogenicity. *Bulletin of the American Physical Society*, 63, 2018.

[46] A. Molteni, Z. P. H. Masri, K. W. Q. Low, H. N. Yousef, J. Sienz, and K. H. Fraser. Experimental measurement and numerical modelling of dye washout for investigation of blood residence time in ventricular assist devices. *The International journal of artificial organs*, 41(4):201–212, 2018.

[47] V. K. Chivukula, J. A. Beckman, A. R. Prisco, T. Dardas, S. Lin, J. W. Smith, N. A. Mokadam, A. Aliseda, and C. Mahr. Left ventricular assist device inflow cannula angle and thrombosis risk. *Circulation: Heart Failure*, 11(4):e004325, 2018.

[48] S. Scardulla, S. Pasta, L. D'Acquisto, S. Sciacca, V. Agnese, C. Vergara, A. Quarteroni, F. Clemenza, D. Bellavia, and Pilato M. Shear stress alterations in the celiac trunk of patients with continuous-flow left ventricular assist device by in-silico and in-vitro flow analysis. *Journal of Heart and Lung Transplantation*, 36(8):906–913, 2017.

[49] M. Perschall, J. B. Drevet, T. Schenkel, and H. Oertel. The progressive wave pump: numerical multiphysics investigation of a novel pump concept with potential to ventricular assist device application. *Artificial organs*, 36(9), 2012.

[50] J. Donea, S. Giuliani, and JP. Halleux. An arbitrary lagrangian-eulerian finite element method for transient dynamic fluid-structure interactions. *Computer methods in applied mechanics and engineering*, 33(1-3):689–723, 1982.

[51] T. J. R. Hughes, W. K. Liu, and T. K. Zimmermann. Lagrangian-Eulerian finite element formulation for incompressible viscous flows. *Computer methods in applied mechanics and engineering*, 29(3):329–349, 1981.

[52] T. J. R. Hughes and G. M. Hulbert. Space-time finite element methods for elastodynamics: formulations and error estimates. *Computer methods in applied mechanics and engineering*, 66(3):339–363, 1988.

[53] H. Nguyen and J. Reynen. A space-time least-square finite element scheme for advection-diffusion equations. *Computer Methods in Applied Mechanics and Engineering*, 42(3):331–342, 1984.

[54] C. Peskin. Flow patterns around heart valves: a digital computer method for solving the equations of motion. *IEEE Transactions on Biomedical Engineering*, (4):316–317, 1973.

[55] D. Boffi and L. Gastaldi. The immersed boundary method: a finite element approach. In *Computational Fluid and Solid Mechanics 2003*, pages 1263–1266. Elsevier, 2003.

[56] L. T. Zhang and M. Gay. Immersed finite element method for fluid-structure interactions. *Journal of Fluids and Structures*, 23(6):839–857, 2007.

[57] R. Glowinski, TW. Pan, and J. Periaux. A fictitious domain method for dirichlet problem and applications. *Computer Methods in Applied Mechanics and Engineering*, 111(3-4):283–303, 1994.

[58] R. Glowinski, TW. Pan, and J. Periaux. A fictitious domain method for external incompressible viscous flow modeled by navier-stokes equations. *Computer Methods in Applied Mechanics and Engineering*, 112(1-4):133–148, 1994.

[59] F. Bertrand, P. A. Tanguy, and F. Thibault. A three-dimensional fictitious domain method for incompressible fluid flow problems. *International Journal for Numerical Methods in Fluids*, 25(6):719–736, 1997.

[60] E. Burman and M. A. Fernández. An unfitted Nitsche method for incompressible fluid–structure interaction using overlapping meshes. *Computer Methods in Applied Mechanics and Engineering*, 279:497–514, 2014.

[61] A. Massing, M. Larson, A. Logg, and M. Rognes. A Nitsche-based cut finite element method for a fluid-structure interaction problem. *Communications in Applied Mathematics and Computational Science*, 10(2):97–120, 2015.

[62] F. Alauzet, B. Fabrèges, M. A. Fernández, and M. Landajuela. Nitsche-XFEM for the coupling of an incompressible fluid with immersed thin-walled structures. *Computer Methods in Applied Mechanics and Engineering*, 301:300–335, 2016.

[63] P. F. Antonietti, M. Verani, C. Vergara, and S. Zonca. Numerical solution of fluid-structure interaction problems by means of a high order Discontinuous Galerkin method on polygonal grids. *Finite Elements in Analysis and Design*, 159:1–14, 2019.

[64] A. Hansbo and P. Hansbo. An unfitted finite element method, based on nitsche's method, for elliptic interface problems. *Computer methods in applied mechanics and engineering*, 191(47-48):5537–5552, 2002.

[65] A. Gerstenberger. *An XFEM based fixed-grid approach to fluid-structure interaction*. PhD thesis, Technische Universität München, 2010.

[66] A. Gerstenberger and W. A. Wall. An extended finite element method/Lagrange multiplier based approach for fluid–structure interaction. *Computer Methods in Applied Mechanics and Engineering*, 197(19-20):1699–1714, 2008.

[67] S. Zonca, C. Vergara, and L. Formaggia. An unfitted formulation for the interaction of an incompressible fluid with a thick structure via an XFEM/DG approach. *SIAM Journal on Scientific Computing*, 40(1):B59–B84, 2018.

[68] C. Vergara and S. Zonca. *Extended Finite Elements Method for Fluid-Structure Interaction with an Immersed Thick Non-linear Structure*, pages 209–243. 01 2018.

[69] C. N. Botterbusch, S. Lucquin, P. Monticone, J. B. Drevet, A. Guignabert, and P. Meneroud. Implantable pump system having an undulating membrane, 2018. US Patent 9,968,720.

[70] M. Hillairet and T. Takahashi. Collisions in three-dimensional fluid structure interaction problems. *SIAM Journal on Mathematical Analysis*, 40(6):2451–2477, 2009.

[71] C. J. Cawthorn and N. J. Balmforth. Contact in a viscous fluid. Part 1. A falling wedge. *Journal of Fluid Mechanics*, 646:327–338, 2010.

[72] U. M. Mayer, A. Popp, A. Gerstenberger, and W. A. Wall. 3D fluid–structure-contact interaction based on a combined XFEM FSI and dual mortar contact approach. *Computational Mechanics*, 46(1):53–67, 2010.

[73] J. Bonet and J. Peraire. An alternating digital tree (ADT) algorithm for 3D geometric searching and intersection problems. *International Journal for Numerical Methods in Engineering*, 31(1):1–17, 1991.

[74] R. Temam. *Navier-Stokes equations: Theory and numerical analysis*, volume 2. 1977.

[75] D. A. Di Pietro and A. Ern. *Mathematical aspects of discontinuous Galerkin methods*, volume 69. Springer Science & Business Media, 2011.

[76] E. Burman, M. A. Fernández, and P. Hansbo. Continuous interior penalty finite element method for Oseen's equations. *SIAM journal on numerical analysis*, 44(3):1248–1274, 2006.

[77] E. Burman. Ghost penalty. *Comptes Rendus Mathematique*, 348(21-22):1217–1220, 2010.

[78] D. N. Arnold, F. Brezzi, B. Cockburn, and L. D. Marini. Unified analysis of discontinuous Galerkin methods for elliptic problems. *SIAM journal on numerical analysis*, 39(5):1749–1779, 2002.

[79] T. Tronchin. Experimental and numerical characterization of vortex mechanisms of lift generation on a wing in flapping motion. 06 2013.

[80] W. Chiu, M. J. Slepian, and D. Bluestein. Thrombus formation patterns in the heartmate ii vad-clinical observations can be predicted by numerical simulations. *ASAIO journal (American Society for Artificial Internal Organs: 1992)*, 60(2):237, 2014.

[81] K. H. Fraser, T. Zhang, M. E. Taskin, B. P. Griffith, and Z. J. Wu. Computational fluid dynamics analysis of thrombosis potential in left ventricular assist device drainage cannulae. *ASAIO journal (American Society for Artificial Internal Organs: 1992)*, 56(3):157, 2010.

[82] RMC So, I Jadic, and MP Mignolet. Fluid–structure resonance produced by oncoming alternating vortices. *Journal of Fluids and Structures*, 13(4):519–548, 1999.

[83] U. K. Müller, E. J. Stamhuis, and J. J. Videler. Riding the Waves: the Role of the Body Wave in Undulatory Fish Swimming1. *Integrative and Comparative Biology*, 42(5):981–987, 11 2002.

MOX Technical Reports, last issues

Dipartimento di Matematica
Politecnico di Milano, Via Bonardi 9 - 20133 Milano (Italy)

38/2020   Sollini, M.; Kirienko, M.; Cavinato, L.; Ricci, F.; Biroli, M.; Ieva, F.; Calderoni, L.; Tabacchi,
Methodological framework for radiomics applications in Hodgkin's lymphoma

34/2020   Antonietti, P.F.; Mazzieri, I.; Nati Poltri, S.
A high-order discontinuous Galerkin method for the poro-elasto-acoustic problem on polygonal and polyhedral grids

35/2020   Morbiducci, U.; Mazzi, V.; Domanin, M.; De Nisco, G.; Vergara, C.; Steinman, D.A.; Gallo, D
Wall shear stress topological skeleton independently predicts long-term restenosis after carotid bifurcation endarterectomy

36/2020   Pellagatti, M.; Masci, C.; Ieva, F.; Paganoni A.M.
Generalized Mixed-Effects Random Forest: a flexible approach to predict university student dropout

37/2020   Fumagalli, A.; Scotti, A.
A mathematical model for thermal single-phase flow and reactive transport in fractured porous media

31/2020   Bernardi, M.S.; Africa, P.C.; de Falco, C.; Formaggia, L.; Menafoglio, A.; Vantini, S.
On the Use of Interfeometric Synthetic Aperture Radar Data for Monitoring and Forecasting Natural Hazards

32/2020   Menafoglio, A.; Sgobba, S.; Lanzano, G.; Pacor, F.
Simulation of seismic ground motion fields via object-oriented spatial statistics: a case study in Northern Italy

33/2020   Centofanti, F.; Fontana, M.; Lepore, A.; Vantini, S.
Smooth LASSO Estimator for the Function-on-Function Linear Regression Model

29/2020   Piersanti, R.; Africa, P.C.; Fedele, M.; Vergara, C.; Dede', L.; Corno, A.F.; Quarteroni, A.
Modeling cardiac muscle fibers in ventricular and atrial electrophysiology simulations

30/2020   Massi, M.C., Gasperoni, F., Ieva, F., Paganoni, A.M., Zunino, P., Manzoni, A., Franco, N.R., e
A deep learning approach validates genetic risk factors for late toxicity after prostate cancer radiotherapy in a REQUITE multinational cohort